SUPPORTING INFORMATION FOR

Impact of Solvated Hydronium Ions and Local pH on H_2O_2 Direct Synthesis over Pd Catalysts Supported on Brønsted Acid Solids

Tomas Ricciardulli,[†,1] Sucharita Vijayarghavan,[†,2] Jason S. Adams,[1] David W. Flaherty[2*]

[1]Department of Chemical and Biomolecular Engineering, University of Illinois Urbana-Champaign, Urbana, IL 61801

[2]School of Chemical and Biomolecular Engineering, Georgia Institute of Technology, Atlanta, GA, 30032

†Equal Contribution

*Corresponding author: dflaherty3@gatech.edu

Section S1. Determination of Pd nanoparticle size in different supports

The nanoparticle size and particle size distribution for each sample was estimated through transmission electron microscopy (TEM; FEI, Tecnai F30) operating at 300 kV. Each sample was ground to a fine powder and dispersed in acetone. Copper-holey carbon TEM grids (200 mesh, SPI supplies) were dispersed in the acetone solution containing the catalyst samples and dried in air at room temperature (293 K). A minimum of 20 nanoparticles were averaged for each sample, and the number averaged mean diameter ($<d>_N$) was calculated by taking a numerical average of these measurements. The surface-averaged mean diameter ($<d>_S$) was calculated according to,

$$\langle d \rangle_S = \frac{\sum_{i=1}^{N} d_i^3}{\sum_{i=1}^{N} d_i^2} \tag{S1.1}$$

where d_i is the measured diameter of each nanoparticle i, and N is the total number of nanoparticles measured. Figure S2 shows representative TEM images and the particle size distribution as an inset for all the samples examined in the study post reduction treatment at 773 K (20 kPa H_2, 773 K, 1 h). Table 1 in Section 2.1. lists the surface-averaged mean diameter for each sample.

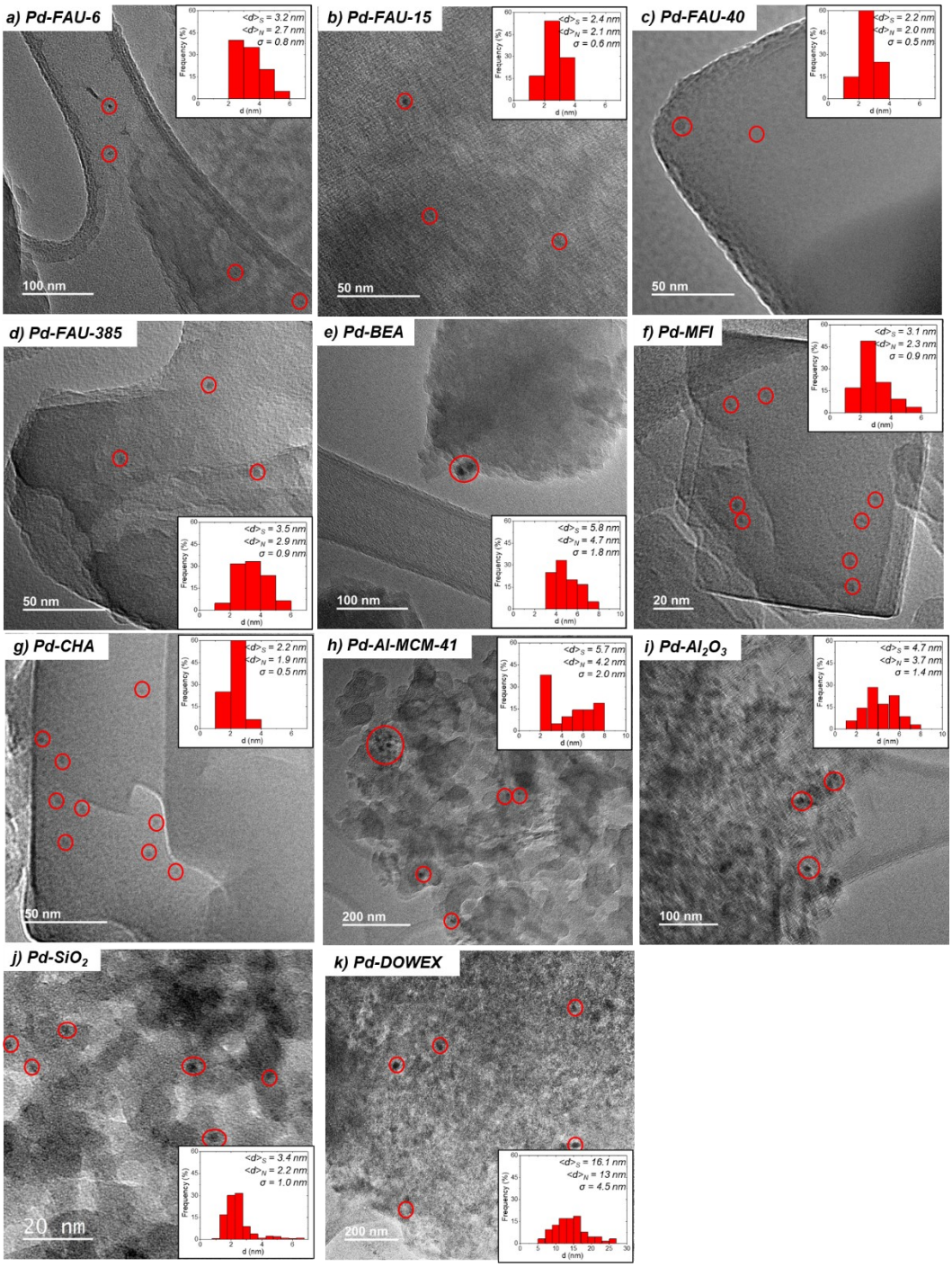

Figure S1. Representative TEM images of Pd nanoparticles on the different supports examined in this study post reduction at 773 K. Nanoparticles are marked with red circles for clarity and inset shows the particle size distribution, average diameters and standard deviation for the respective sample.

Section S2. Determination of Pd dispersion from CO chemisorption

The number of available surface Pd metal atoms for catalysis (or Pd dispersion) was estimated by volumetric CO chemisorption (Micrometrics, 3Flex). Approximately 1 g of sample was loaded into a quartz tube and degassed under vacuum (0.1 kPa) at 573 K for 12 h to remove moisture from the samples before chemisorption measurements. All samples except Pd-DOWEX were heated at 10 K s^{-1} to 573 K in H_2 and held for 1 h, evacuated to less than 0.1 Pa at 573 K and held for 1 h before cooling to ambient temperature (298 K) under vacuum. Pd-DOWEX was degassed under vacuum (0.1 kPa) at 373 K for 3 h to remove water but to not decompose the sulfonic acid resin. It was then heated at 10 K s^{-1} to 373 K in H_2 and held for 1 h, evacuated to less than 0.1 Pa at 573 K and held for 1 h before cooling to 298 K. Two CO chemisorption isotherms between 0.05 and 10 kPa were taken with roughly 10 points with a 10 s equilibration time per measured point on each sample separated by 0.5 h of vacuum. The first isotherm measures the total CO uptake (reversible and irreversible CO adsorption) and the second isotherm measures only the reversible CO uptake. The reported irreversible CO uptake quantities correspond to the y-intercept values of the difference isotherm. A stoichiometry coefficient of 0.5 CO/Pd was used to account for an average of the different binding modes of CO to Pd atoms. [1-4] Table S1 presents the irreversible CO uptake values and calculated Pd dispersion (ratio of moles of surface Pd estimated from irreversible CO uptake to the moles of bulk Pd estimated from ICP-OES Pd weight loading) for all samples from Table 1 of the main text.

Table S1. List of Pd catalysts on different supports used in this study with Si/Al ratio, bulk Pd weight loading, bulk Pd content, irreversible CO uptake from CO chemisorption, calculated Pd dispersion using a stoichiometry coefficient of 0.5 CO/Pd, and estimated Pd diameter from dispersion values. All samples except Pd-DOWEX were reduced *ex situ* at 773 K, and *in situ* at 573 K. Pd-DOWEX was reduced *in situ* at 373 K.

Catalyst	Si/Al	Pd loading (wt%)	Pd content (µmol/g)	Irreversible CO uptake (µmol/g)	Pd dispersion (%)	$<d_{CHEM}>$ (nm)
Pd-FAU	6	0.02	1.88	0.77	82	1.1
Pd-FAU	15	0.02	1.88	0.43	45	2.0
Pd-FAU	40	0.02	1.88	0.48	51	1.8
Pd-FAU	385	0.02	1.88	0.50	53	1.7
Pd-BEA	14	0.02	1.88	0.76	81	1.1
Pd-MFI	11.5	0.02	1.88	0.62	66	1.4
Pd-CHA	30	0.02	1.88	0.66	70	1.3
Pd-Al-MCM-41	10	0.02	1.88	0.47	50	1.8
Pd-γ-Al_2O_3	n/a	0.03	2.82	0.44	31	2.9
Pd-SiO_2	n/a	0.05	4.70	1.72	73	1.2
Pd-DOWEX	n/a	0.05	4.70	0.16	7	12.9

Section S3. Determination of the point of zero charge of oxide supports

The point of zero charge of the catalyst support materials was measured using a technique adapted from Noh and Schwarz. [5] Aliquots (2.5 cm^3) of degassed deionized H_2O (pH = 7) were incrementally added to a large quantity of support material (500 mg). The slurry was degassed with He and pH was measured (Oakton pH 450) as a function of the slurry concentration. The point of zero charge is calculated as the extrapolation of pH to the pore volume of the support. [6]

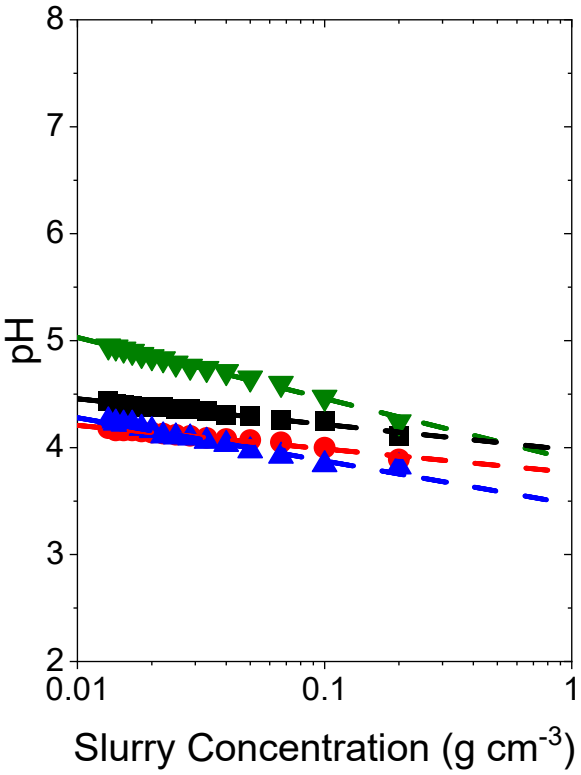

Figure S2. Measurements of pH in degassed slurries of deionized water as a function of the concentration of FAU-6 (black ■), FAU-15 (red ●), FAU-40 (blue ▲), and FAU-385 (green ▼).

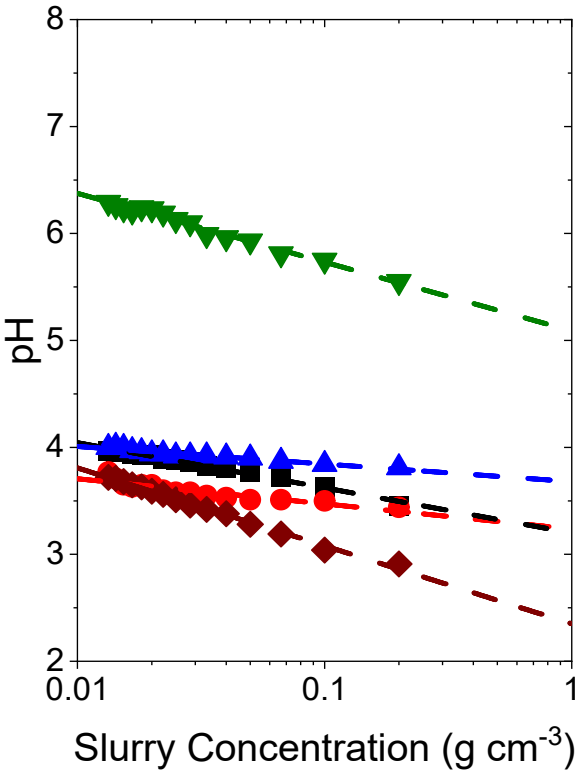

Figure S3. Measurements of pH in degassed slurries of deionized water as a function of the concentration of BEA-14 (black ■), MFI-11.5 (red ●), CHA-30 (blue ▲), Al-MCM-41 (green ▼), and DOWEX 50WX8 (brown ♦).

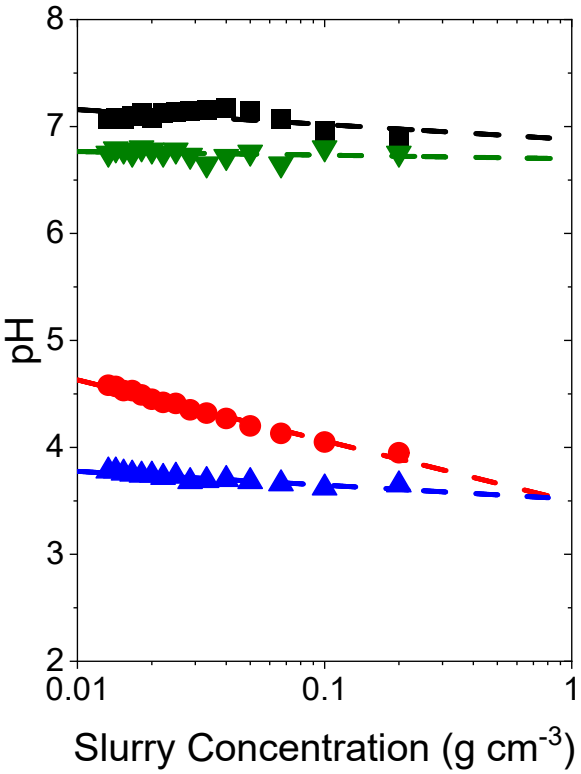

Figure S4. Measurements of pH in degassed slurries of deionized water as a function of the concentration of Davisil 646 SiO_2 (black ■), Cabot Fumed SiO_2 (red ●), US Nano Anatase TiO_2 (blue ▲), and Sasol Catalox γ-Al_2O_3 (green ▼).

Section S4. Testing Mass Transport Limitations

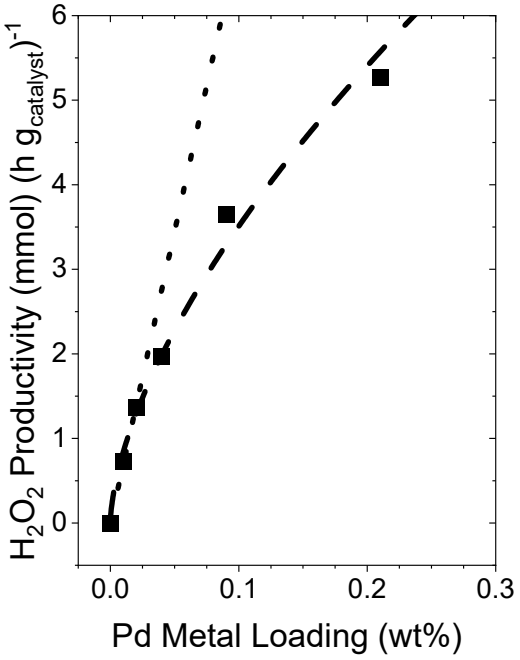

Figure S5. Catalytic H_2O_2 productivity as a function of Pd metal loading on Pd-FAU-15 at the most reactive set of conditions considered in this study (200 kPa H_2, 60 kPa O_2, 296 K). The dashed line indicates a fit to the data, whereas the dotted line reflects H_2O_2 productivity in the absence of mass transfer restrictions.

The microporous nature of zeolitic materials hinders both the diffusion of reactants to and products away from the active sites, which may compound with the limited solubility of reactants (e.g., H_2, O_2) in the H_2O solvent to limit the maximum per-volume reactivity of catalysts. To gauge the impact of transport restrictions on H_2O_2 synthesis, we prepared a series of Pd-FAU-15 catalysts with varied Pd loadings using the same parent H-FAU-15 sample to keep the dimensions and composition of the zeolite support constant. Figure S1 shows H_2O_2 productivity per total mass

catalyst (mol H_2O_2 $g_{catalyst}^{-1}$ h^{-1}) as a function of the Pd metal loading under the conditions that give the greatest rates in this study (200 kPa H_2, 60 kPa O_2, 296 K), and comparisons of these mass averaged rates effectively reveal any form of mass transfer limitation. Mass-averaged H_2O_2 formation rates scale linearly with Pd loading for catalysts with the lowest Pd content (0.04 wt% and below, Si/Pd > 1000), which indicates catalysis proceeds without artifacts from mass transfer effects and H_2O_2 decomposition.[7] Consequently, the Pd-aluminosilicates examined in the remainder of this study were synthesized to 0.02 wt% Pd (Table 1).

Section S5. Supplementary Kinetic Data

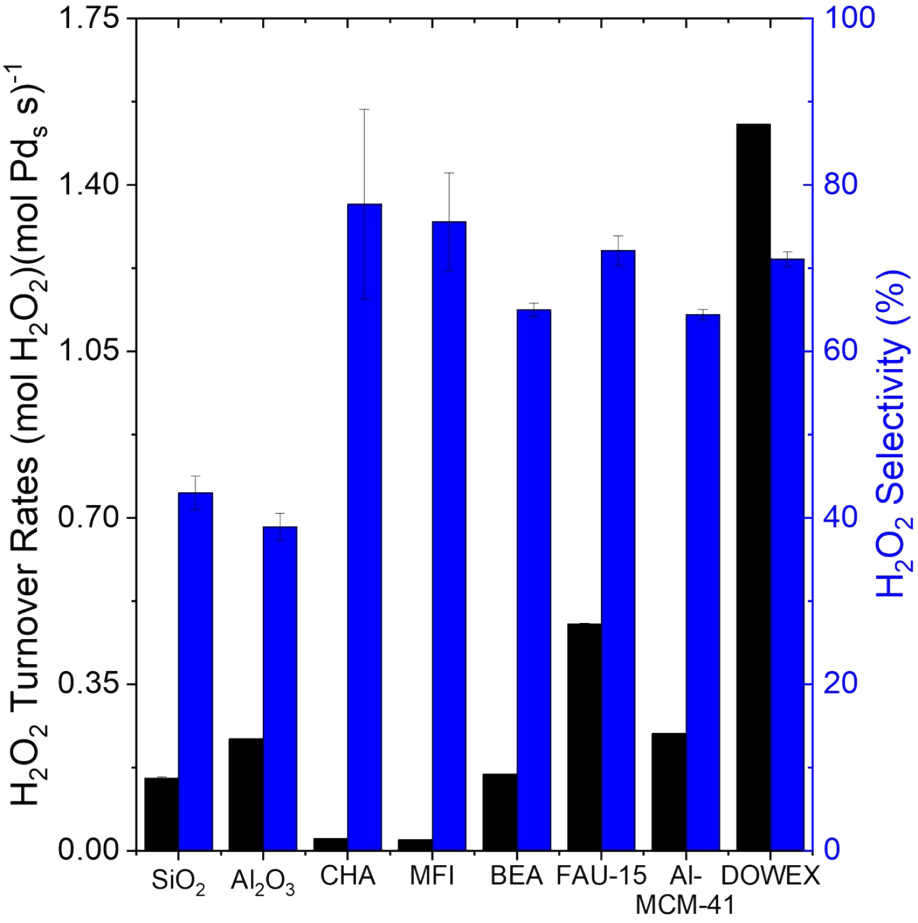

Figure S6. H_2O_2 turnover rates normalized by surface Pd calculated from CO chemisorption (black) and selectivities (blue) for Pd catalysts on different supports at standard reaction conditions (200 kPa H_2, 60 kPa O_2, 286 K).

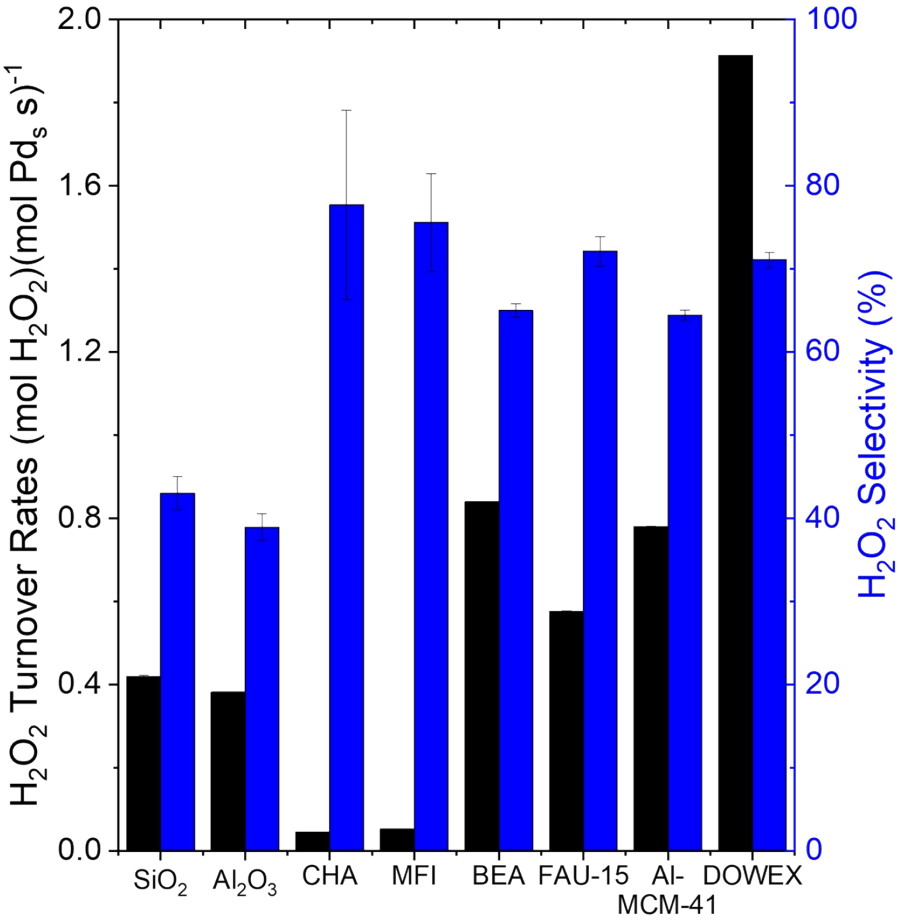

Figure S7. H_2O_2 turnover rates normalized by surface Pd calculated from TEM nanoparticle sizes (black) and selectivities (blue) for Pd catalysts on different supports at standard reaction conditions (200 kPa H_2, 60 kPa O_2, 286 K).

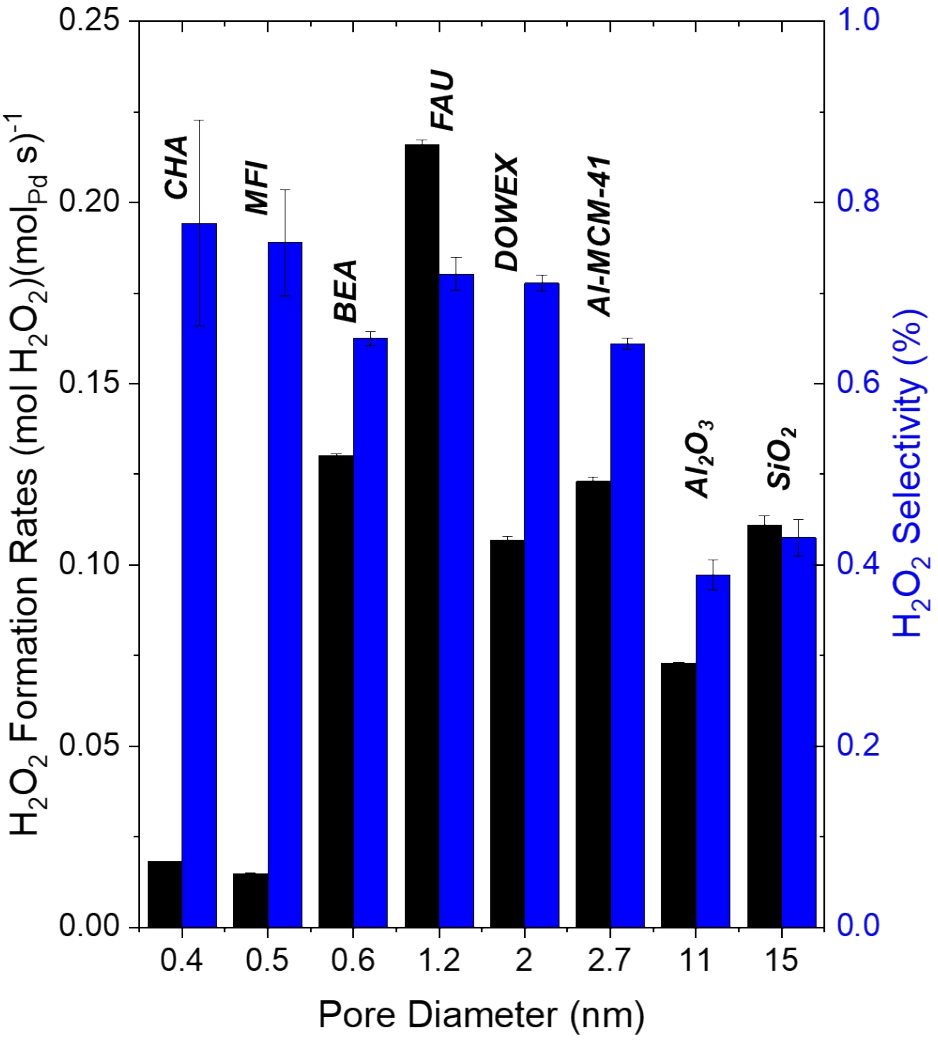

Figure S8. H_2O_2 formation rates (black) and selectivities (blue) for Pd catalysts on different supports as a function of support pore diameter at standard reaction conditions (200 kPa H_2, 60 kPa O_2, 286 K).

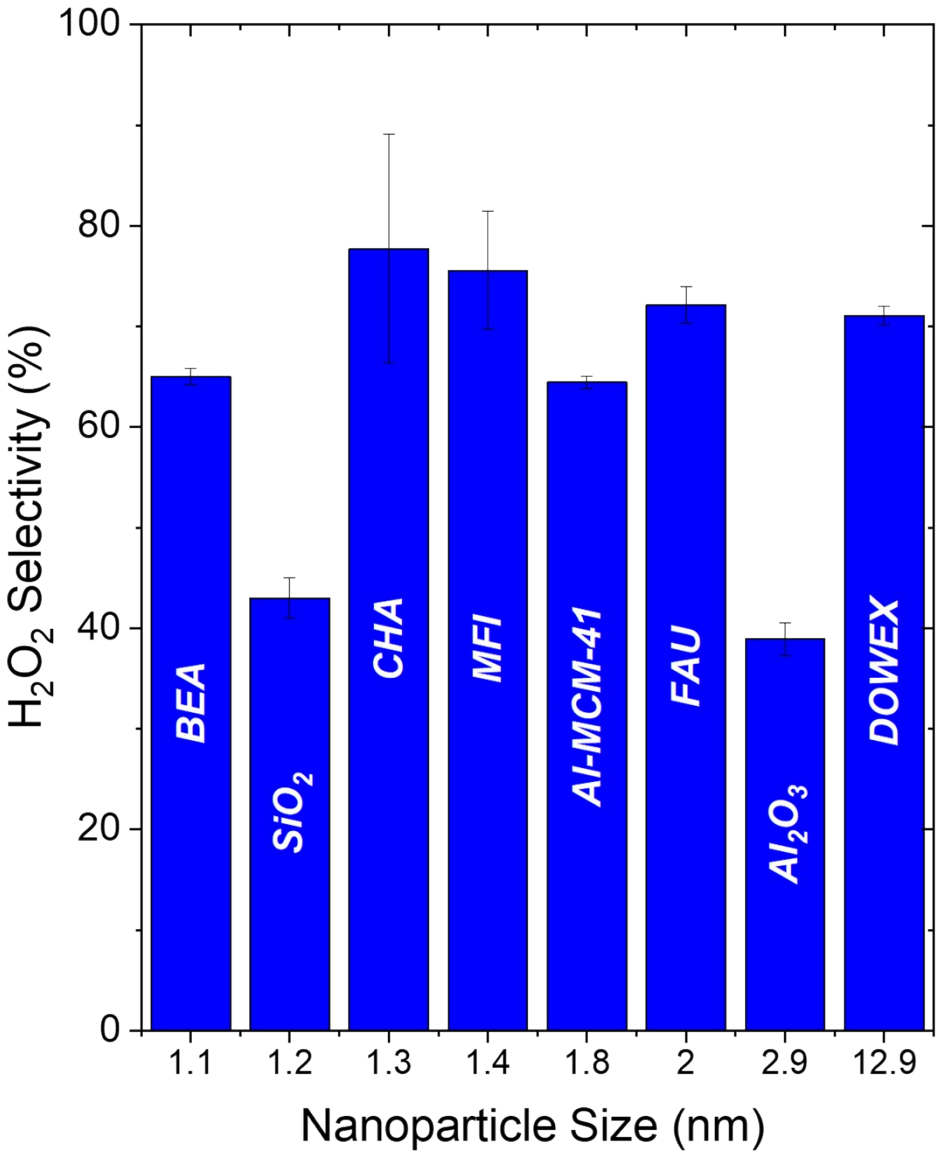

Figure S9. H_2O_2 selectivities for Pd catalysts on different supports as a function of nanoparticle size estimated from Pd dispersion values calculated from CO chemisorption at standard reaction conditions (200 kPa H_2, 60 kPa O_2, 286 K).

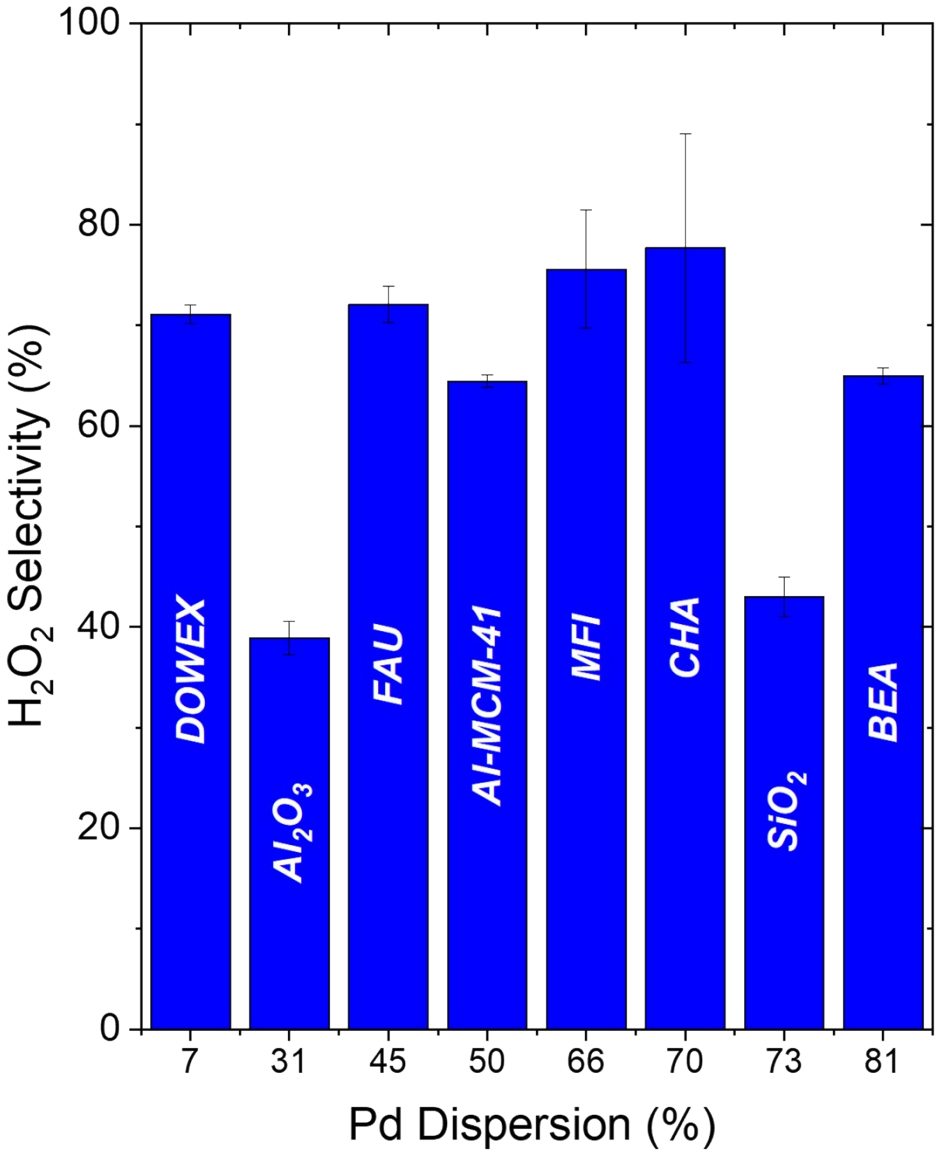

Figure S10. H_2O_2 selectivities for Pd catalysts on different supports as a function of Pd dispersion calculated from irreversible CO uptake from CO chemisorption at standard reaction conditions (200 kPa H_2, 60 kPa O_2, 286 K).

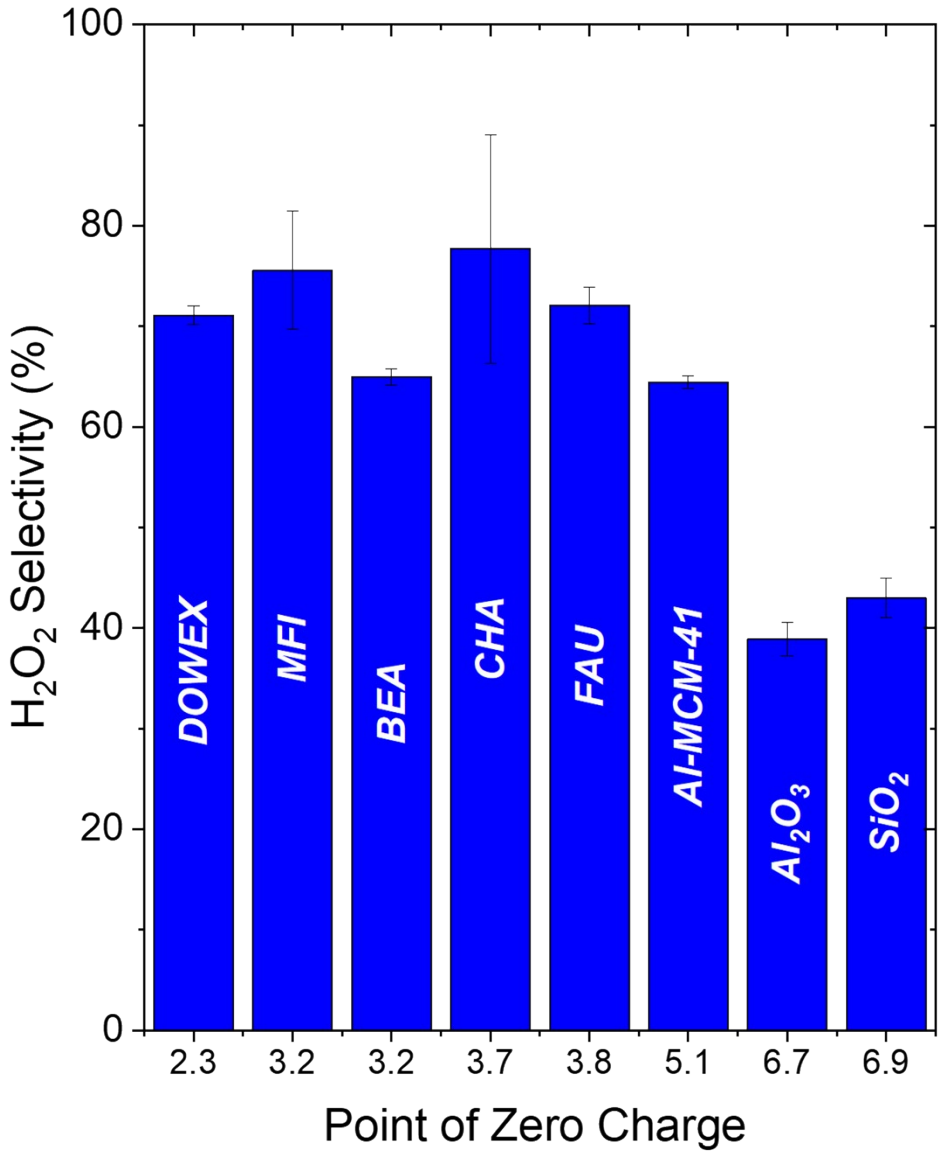

Figure S11. H_2O_2 selectivities for Pd catalysts on different supports as a function of point of zero charge of the support (Table 1) at standard reaction conditions (200 kPa H_2, 60 kPa O_2, 286 K).

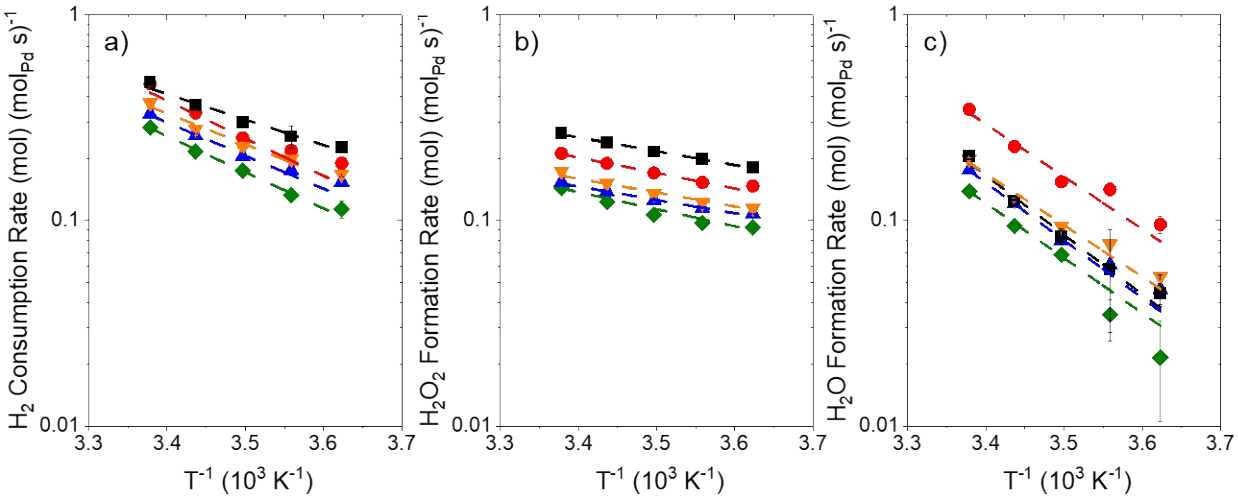

Figure S12. Arrhenius plots at 200 kPa H_2, 60 kPa O_2 for (a) H_2 consumption, (b) H_2O_2 formation, and (c) H_2O formation on Pd-FAU-15 after oxidation at 823 K (green ♦), reduction at 473 K (red ●), reduction at 573 K (blue ▲), reduction at 673 K (orange ▼), and reduction at 773 K (black ■).

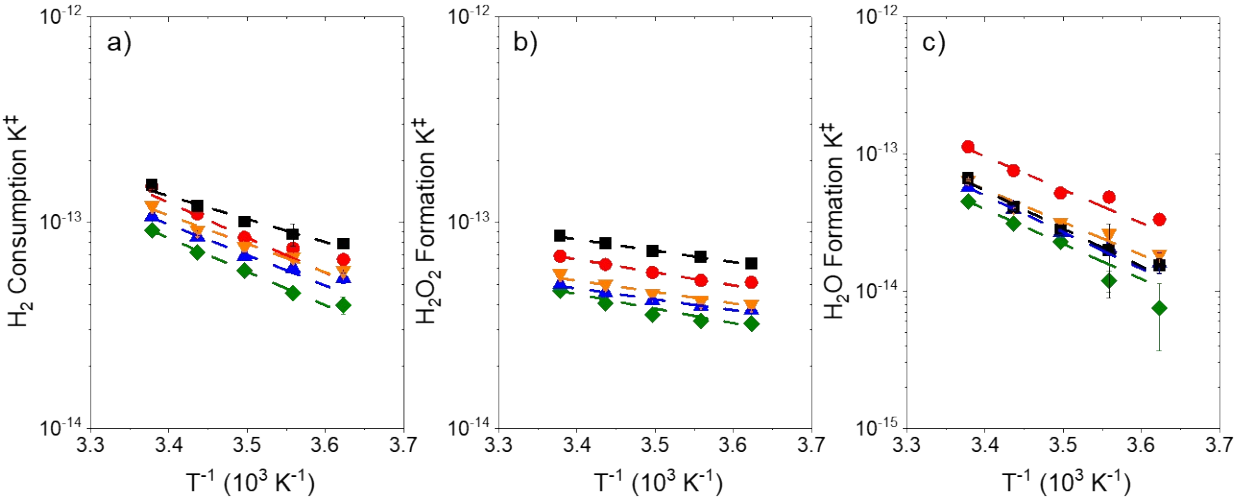

Figure S13. Eyring-Polanyi plots at 200 kPa H_2, 60 kPa O_2 for (a) H_2 consumption, (b) H_2O_2 formation, and (c) H_2O formation on Pd-FAU-15 after oxidation at 823 K (green ♦), reduction at 473 K (red ●), reduction at 573 K (blue ▲), reduction at 673 K (orange ▼), and reduction at 773 K (black ■).

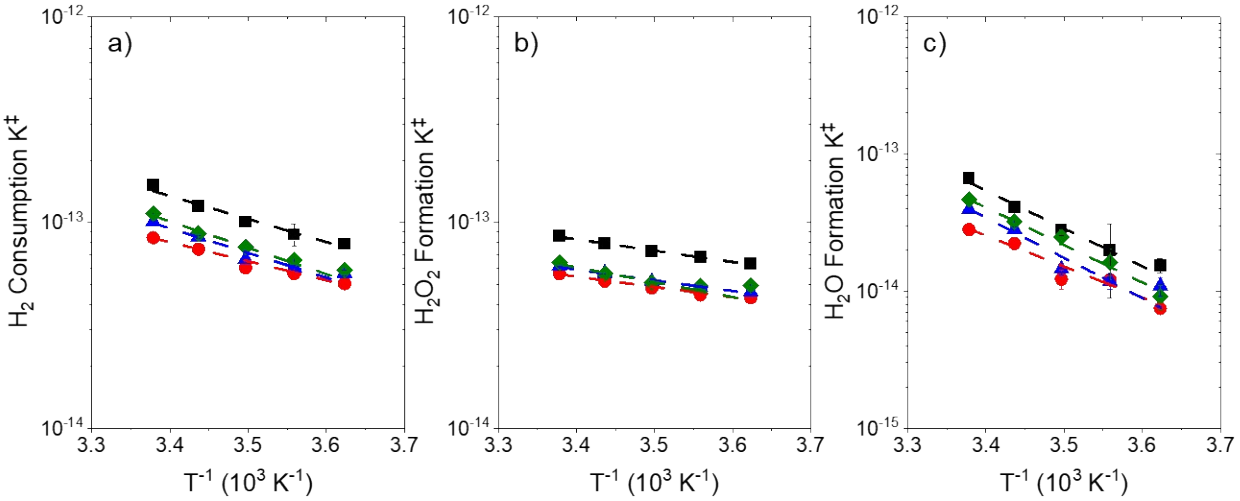

Figure S14. Arrhenius plots at 200 kPa H_2, 60 kPa O_2 for (a) H_2 consumption, (b) H_2O_2 formation, and (c) H_2O formation on Pd-FAU-6 (red ●), Pd-FAU-15 (black ■), Pd-FAU-40 (blue ▲), and Pd-FAU-385 (green ♦). Catalysts were reduced at 773 K *ex situ* prior to measurement.

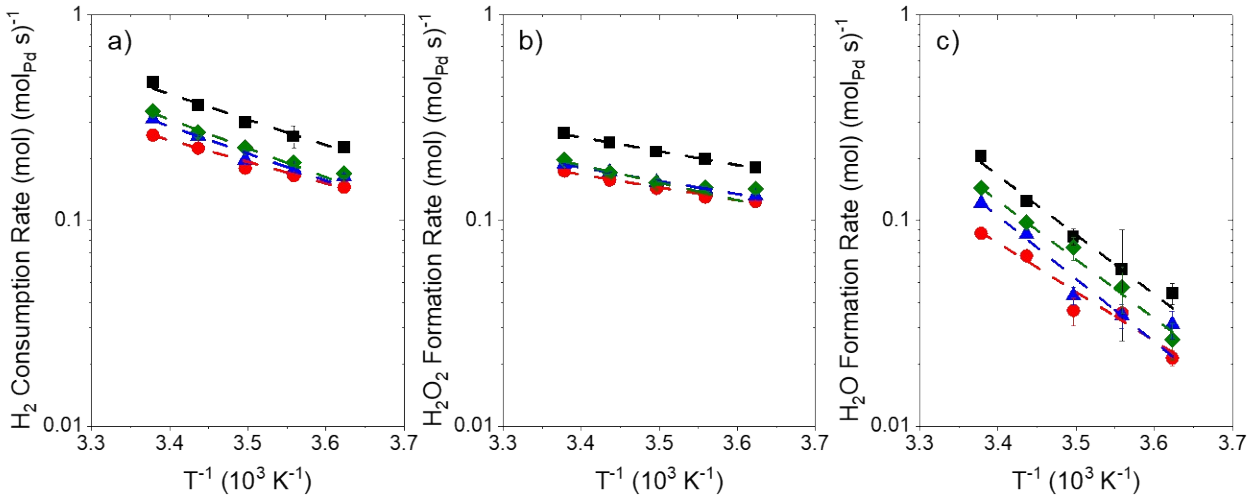

Figure S15. Eyring-Polanyi plots at 200 kPa H_2, 60 kPa O_2 for (a) H_2 consumption, (b) H_2O_2 formation, and (c) H_2O formation on Pd-FAU-6 (red ●), Pd-FAU-15 (black ■), Pd-FAU-40 (blue ▲), and Pd-FAU-385 (green ♦). Catalysts were reduced at 773 K *ex situ* prior to measurement.

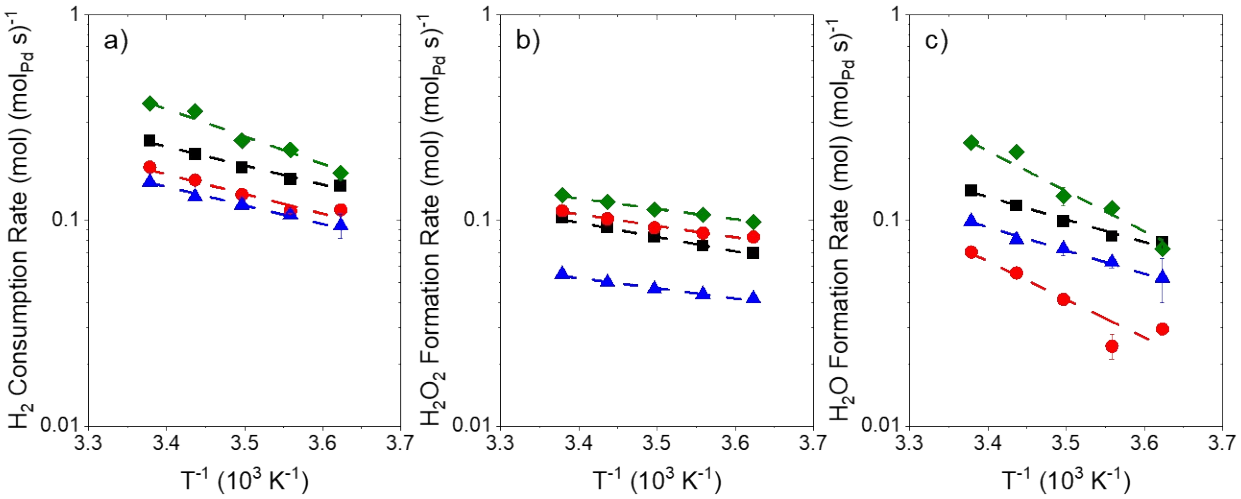

Figure S16. Arrhenius plots at 200 kPa H_2, 60 kPa O_2 for (a) H_2 consumption, (b) H_2O_2 formation, and (c) H_2O formation on Pd-SiO_2 (black ■), Pd-SiO_2 mixed with DOWEX 50WX8 (red ●), Pd-Al_2O_3 (blue ▲) and Pd-Al_2O_3 mixed with FAU-15 (green ♦).

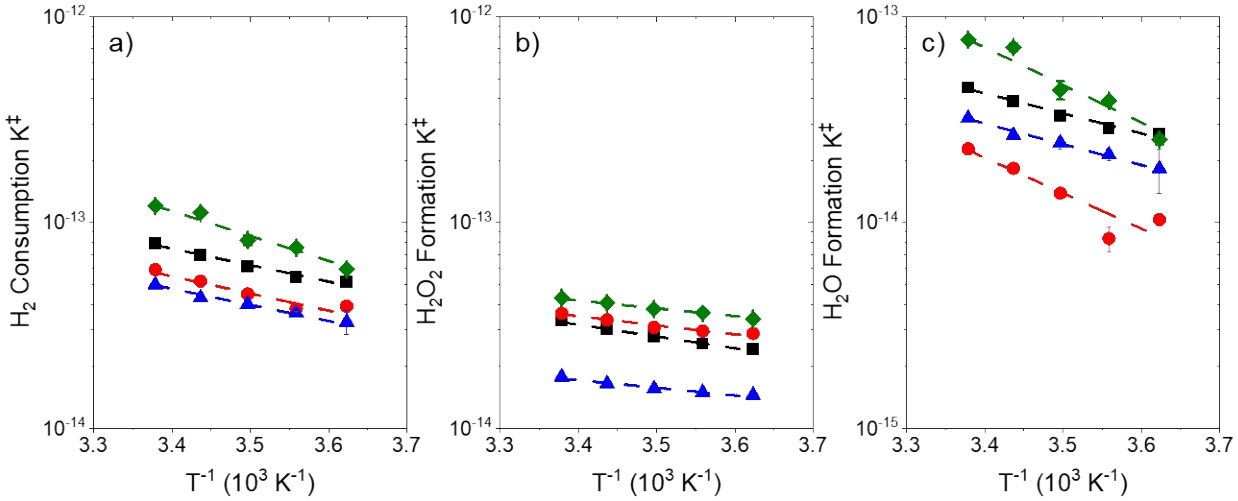

Figure S17. Eyring-Polanyi plots at 200 kPa H_2, 60 kPa O_2 for (a) H_2 consumption, (b) H_2O_2 formation, and (c) H_2O formation on Pd-SiO_2 (black ■), Pd-SiO_2 mixed with DOWEX 50WX8 (red ●), Pd-Al_2O_3 (blue ▲) and Pd-Al_2O_3 mixed with FAU-15 (green ♦).

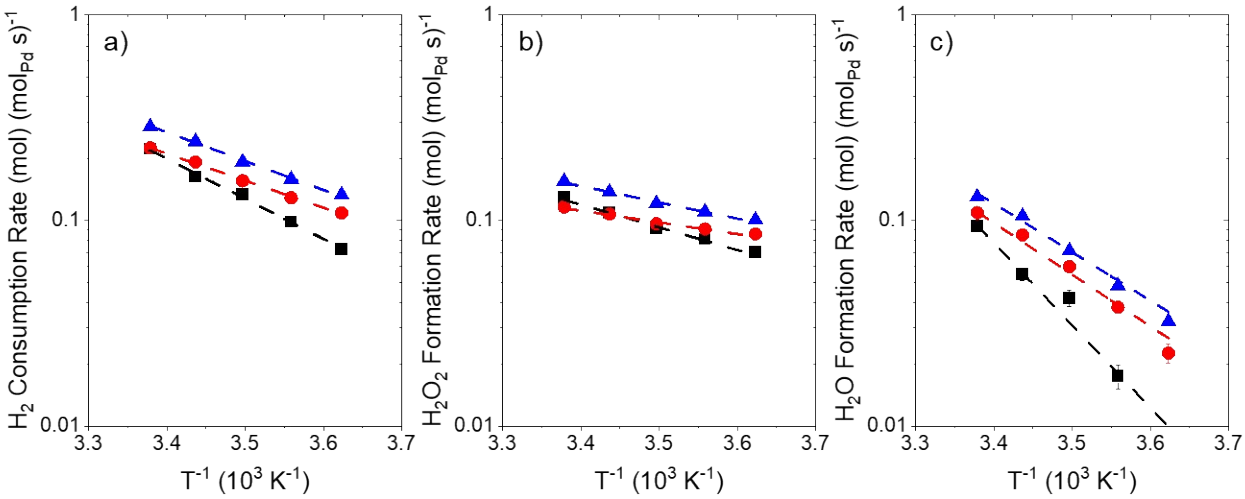

Figure S18. Arrhenius plots at 200 kPa H_2, 60 kPa O_2 for (a) H_2 consumption, (b) H_2O_2 formation, and (c) H_2O formation on Pd-DOWEX 50WX8 (black ■), Pd-MCM-41 (red ●), Pd-BEA-14 (blue ▲). The Pd-MCM-41 and Pd-BEA-14 catalysts were reduced at 773 K *ex situ* prior to measurement.

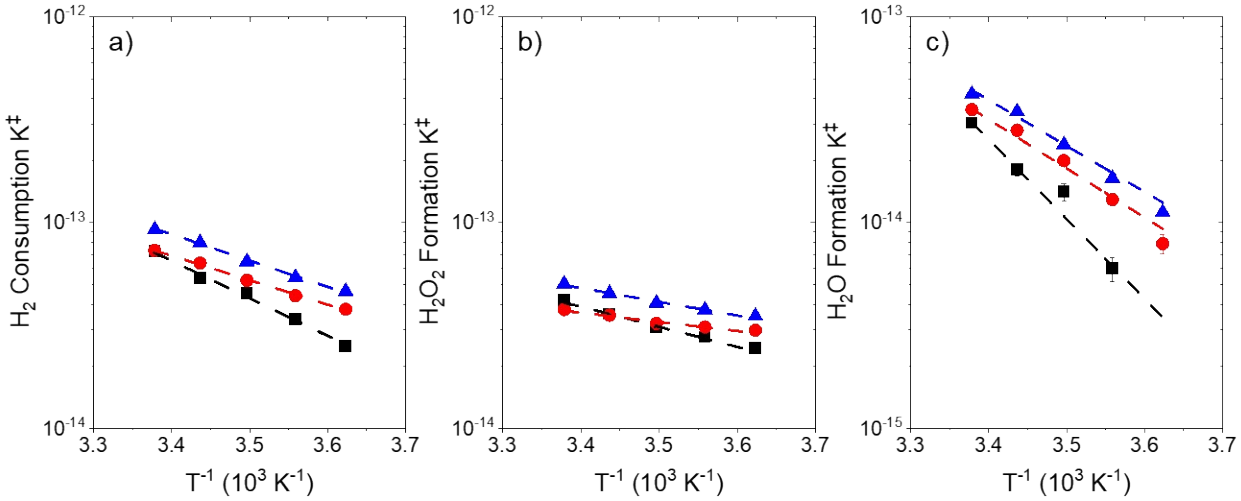

Figure S19. Eyring-Polanyi plots at 200 kPa H_2, 60 kPa O_2 for (a) H_2 consumption, (b) H_2O_2 formation, and (c) H_2O formation on Pd-DOWEX 50WX8 (black ■), Pd-MCM-41 (red ●), Pd-BEA-14 (blue ▲). The Pd-MCM-41 and Pd-BEA-14 catalysts were reduced at 773 K *ex situ* prior to measurement.

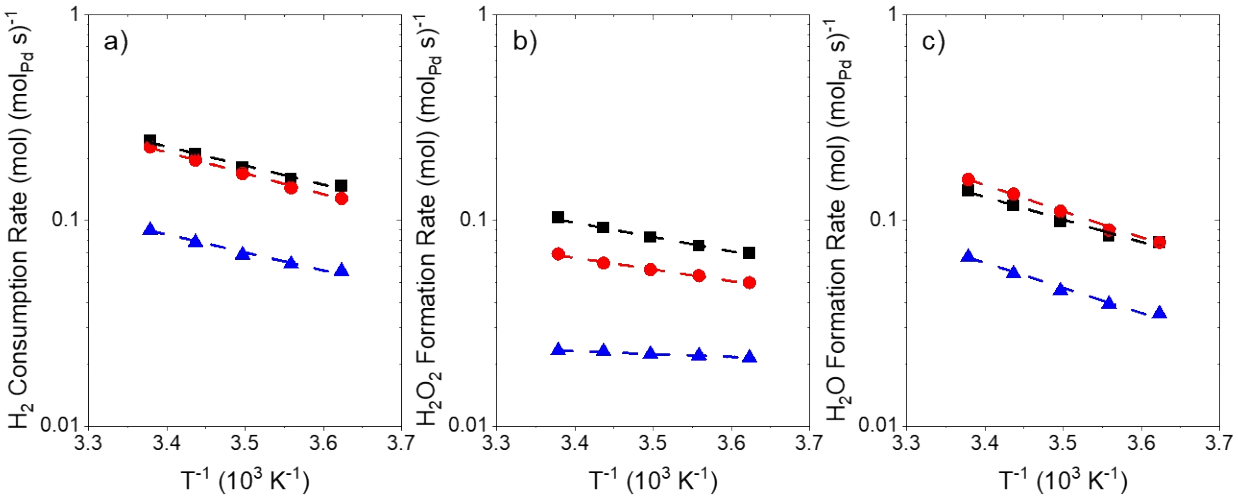

Figure S20. Arrhenius plots at 200 kPa H_2, 60 kPa O_2 for (a) H_2 consumption, (b) H_2O_2 formation, and (c) H_2O formation on Pd-SiO_2 (black ■), Pd-Fumed SiO_2 (red ●), and Pd-TiO_2 (blue ▲).

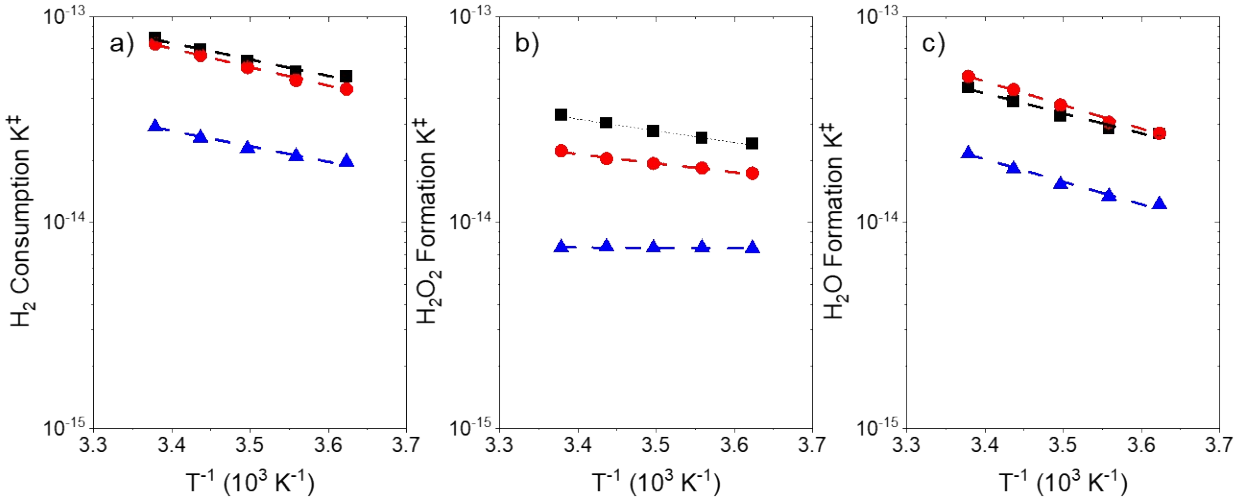

Figure S21. Eyring-Polanyi plots at 200 kPa H_2, 60 kPa O_2 for (a) H_2 consumption, (b) H_2O_2 formation, and (c) H_2O formation on Pd-SiO_2 (black ■), Pd-Fumed SiO_2 (red ●), and Pd-TiO_2 (blue ▲).

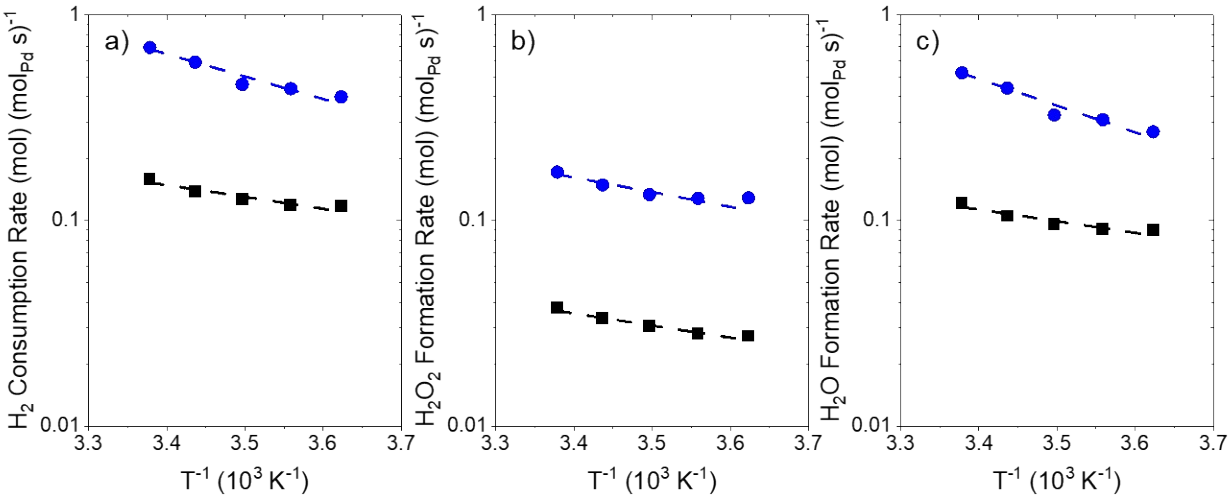

Figure S22. Arrhenius plots at 55 kPa H_2, 80 kPa O_2 for (a) H_2 consumption, (b) H_2O_2 formation, and (c) H_2O formation on Pd-FAU-15 (black ■) and Pd-SiO_2 (blue ●).

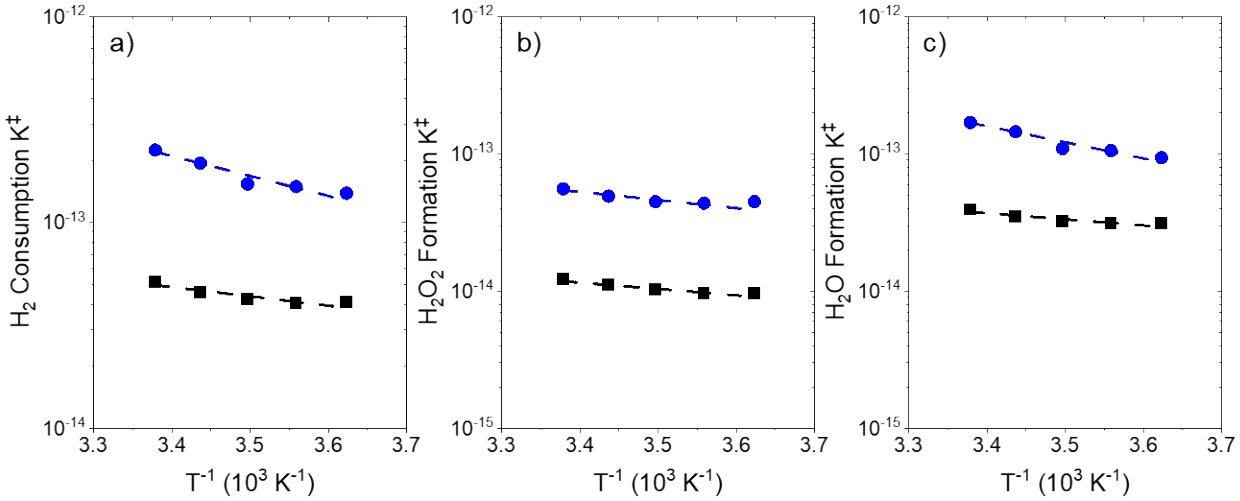

Figure S23. Eyring-Polanyi plots at 55 kPa H_2, 80 kPa O_2 for (a) H_2 consumption, (b) H_2O_2 formation, and (c) H_2O formation on Pd-FAU-15 (black ■) and Pd-SiO_2 (blue ●).

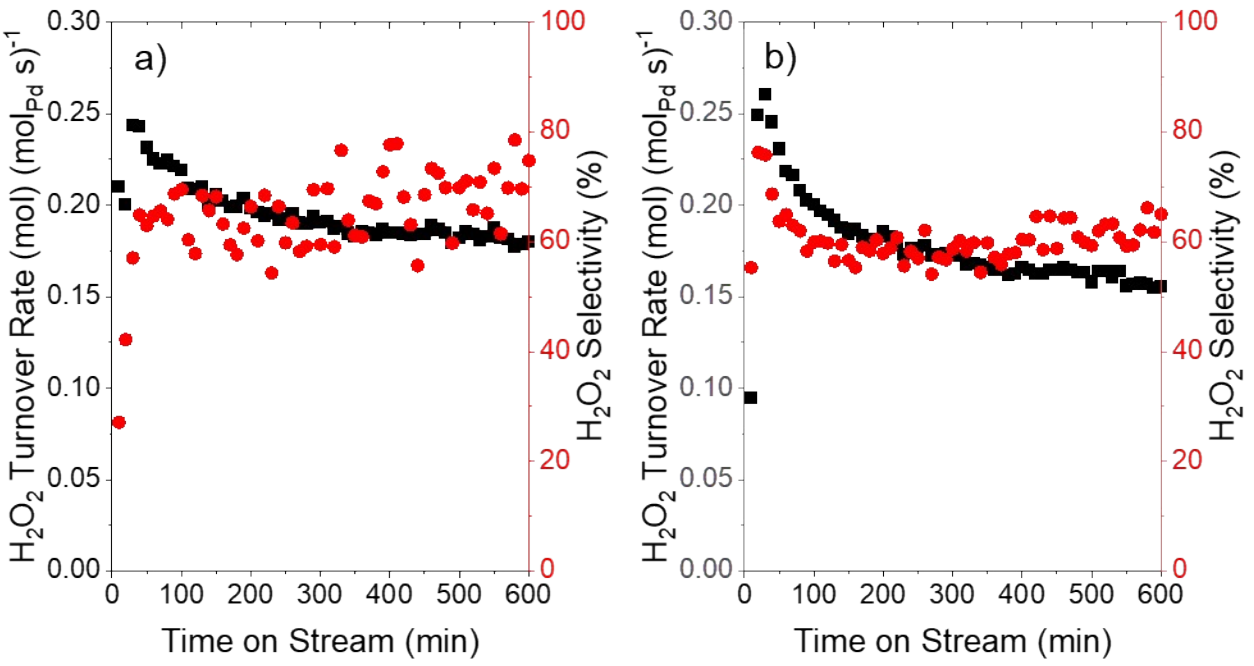

Figure S24. H_2O_2 turnover rates (black ■) and selectivities (red ●) as a function of time-on-stream for (a) Pd-FAU-15 and (b) Pd-BEA-14 at 200 kPa O_2, 60 kPa O_2, 286 K. Catalysts were reduced at 773 K *ex situ* prior to measurement.

Section S6. Mechanism Derivation for Reactions among H_2 and O_2 on Pd Nanoparticles

$$H_2 + 2^{\#} \rightleftharpoons 2H^{\#} \quad (1)$$

$$O_2 + * \rightleftharpoons O_2* \quad (2)$$

$$O_2* + H^{\#} + H_2O \longrightarrow OOH* + H_2O + {}^{\#} \quad (3)$$

$$OOH* + H^{\#} + H_2O \longrightarrow H_2O_2* + H_2O + {}^{\#} \quad (4)$$

$$OOH* + H^{\#} + H_2O \longrightarrow O* + 2H_2O + {}^{\#} \quad (5)$$

$$O* + H^{\#} + H_2O \longrightarrow OH* + H_2O + {}^{\#} \quad (6)$$

$$OH* + H^{\#} + H_2O \longrightarrow H_2O* + H_2O + {}^{\#} \quad (7)$$

$$H_2O_2* + H^{\#} + H_2O \longrightarrow OH* + 2H_2O + {}^{\#} \quad (8)$$

$$H_2O_2 + * \rightleftharpoons H_2O_2* \quad (9)$$

$$H_2O + * \rightleftharpoons H_2O* \quad (10)$$

Scheme S1. Proposed system of elementary steps describing H_2O_2 and H_2O formation on metal catalysts. The symbol $\longrightarrow$ denotes an irreversible reaction, whereas $\rightleftharpoons$ signifies a reversible reaction and $\rightleftharpoons$ corresponds to a quasi-equilibrated reaction.

The following mechanism derivation is based on prior works[8-11] that showed that the kinetically relevant H_2 consumption ($-r_{H_2}$) limits the total rate of O_2 reduction ($-r_{O_2}$) to form H_2O_2 and H_2O on all the Pd-based catalysts examined.

$$-r_{O_2} = r_3 = \frac{r_{H_2O}}{2} + r_{H_2O_2} \quad (S6.1)$$

Step 3 is identified as the kinetically relevant step which determines the formation rates of H_2O_2 and H_2O ($r_{H_2O_2}$ and r_{H_2O}).

$$r_3 = k_3\left[O_2{}^*\right]\left[H^{\#}\right][H_2O] \tag{S6.2}$$

From Scheme 1 and S1, reactions (2), (9), and (10) are considered to be quasi-equilibrated, which yield the following expressions,

$$[O_2{}^*] = K_2[O_2][*] \tag{S6.3}$$

$$[H_2O_2{}^*] = K_9[H_2O_2][*] \tag{S6.4}$$

$$[H_2O^*] = K_{10}[H_2O][*] \tag{S6.5}$$

In order to estimate coverages of other intermediates – OOH*, O* and OH*, we apply the pseudo steady state hypothesis (PSSH)

$$[OOH^*] = \frac{k_3K_2[O_2][*]}{k_4 + k_5} \tag{S6.6}$$

$$[O^*] = \frac{k_5k_3K_2[O_2][*]}{k_6(k_4 + k_5)} \tag{S6.7}$$

$$\left[OH^*\right] = \frac{k_5k_3K_2[O_2][*]}{k_7(k_4 + k_5)} + \frac{k_8K_9[H_2O_2][*]}{k_7} \tag{S6.8}$$

Steady-state rate and activation enthalpy measurements were performed at 200 kPa H_2 and 60 kPa O_2 which correspond to a limit of high $[H_2]$ to $[O_2]$ ratios where H_2O_2 and H_2O formation rates are independent of H_2 pressure. At these conditions, H_2 activation is more reversible (step 1) and $^{\#}$-sites are saturated by $H^{\#}$. In this case,

$$\left[H^{\#}\right] = \sqrt{K_1[H_2]}\,[\#] \tag{S6.9}$$

We perform site balance on * and # sites,

$$[*]_0 = [*] + \left[O_2{}^*\right] + \left[OOH^*\right] + \left[O^*\right] + \left[OH^*\right] + \left[H_2O^*\right] + \left[H_2O_2{}^*\right] \tag{S6.10}$$

$$[\#]_0 = [\#] + \left[H^\#\right] \tag{S6.11}$$

Substituting coverage expressions for all intermediate species from equations S6.3 through S6.9, we get expressions for empty site coverage for the two sites,

$$[*] = \frac{[*]_0}{1 + K_2[O_2]\left(1 + \frac{k_3}{k_4 + k_5} + \frac{k_5 k_3}{k_4 + k_5}\left(\frac{1}{k_6} + \frac{1}{k_7}\right)\right) + K_9\left(1 + \frac{k_8}{k_7}\right)[H_2O_2] + K_{10}[H_2O]} \tag{S6.12}$$

$$[\#] = \frac{[\#]_0}{1 + \sqrt{K_1[H_2]}} \tag{S6.13}$$

The rates of H_2O_2 and H_2O formation can be written as follows,

$$r_{H_2O_2} = r_4 = k_4[OOH^*][H^\#][H_2O]\left(\frac{1}{[*]_0} + \frac{1}{[\#]_0}\right) \tag{S6.14}$$

$$r_{H_2O} = 2r_5 = 2k_5[OOH^*][H^\#][H_2O]\left(\frac{1}{[*]_0} + \frac{1}{[\#]_0}\right) \tag{S6.15}$$

Substituting coverage terms and [*] and [#] from expressions derived above, and neglecting H_2O_2 concentration since rate measurements were conducted at differential conversions of H_2 and form negligible concentrations of H_2O_2, we can obtain final rate expressions for H_2O_2 and H_2O formation:

$$\frac{r_{H_2O_2}}{[L]} = \frac{\frac{2k_3K_2k_4}{(k_4+k_5)}[H_2O][O_2]}{1+K_2\left(1+\frac{k_3}{k_4+k_5}+\frac{k_5k_3}{k_4+k_5}\left(\frac{1}{k_6}+\frac{1}{k_7}\right)\right)[O_2]} \quad \text{(S6.16)}$$

$$\frac{r_{H_2O}}{[L]} = \frac{\frac{4k_3K_2k_5}{(k_4+k_5)}[H_2O][O_2]}{1+K_2\left(1+\frac{k_3}{k_4+k_5}+\frac{k_5k_3}{k_4+k_5}\left(\frac{1}{k_6}+\frac{1}{k_7}\right)\right)[O_2]} \quad \text{(S6.17)}$$

These expressions state that rates will initially increase with O_2 pressures before approaching constant values under high H_2 pressure conditions where H_2 activation is largely reversible. All rate measurements were performed in a region where rates increase linearly with O_2 pressures, which yields the following rate expressions for H_2O_2 and H_2O formation:

$$r_{H_2O_2} = \frac{k_3k_4K_2}{k_4+2k_5}[O_2] \quad \text{(S6.18)}$$

$$r_{H_2O} = \frac{2k_3k_5K_2}{k_4+2k_5}[O_2] \quad \text{(S6.19)}$$

Following a similar derivation, the rate expressions for H_2O_2 and H_2O formation at low H_2 pressures where rates have a linear dependence on H_2 pressures and H_2 activation is irreversible simplifies to:

$$\frac{r_{H_2O_2}}{[L]} = \frac{k_1k_4[H_2]}{k_4+2k_5} \quad \text{(S6.20)}$$

$$\frac{r_{H_2O_2}}{[L]} = \frac{2k_1k_5[H_2]}{k_4+2k_5} \quad \text{(S6.21)}$$

Section S7. Supplementary Apparent Activation Enthalpy and Entropy

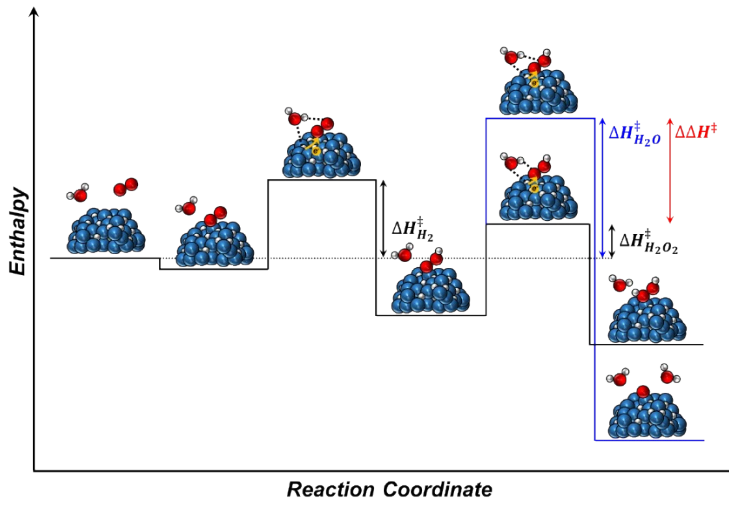

Scheme S2. Qualitative reaction coordinate diagram showing reactions of H_2 and O_2 to form H_2O_2 and H_2O over H-covered Pd nanoparticle surfaces. Spheres represent Pd atoms (blue), oxygen atoms (red), and hydrogen atoms (white).

Scheme S2 shows a qualitative reaction coordinate diagram illustrating the physical significance of the measurable apparent activation enthalpies consistent with the current understanding of the H_2O_2 synthesis mechanism. Apparent activation entropies for ($^{\Delta S^{\ddagger}_{H_2O_2}}$), H_2O formation ($^{\Delta S^{\ddagger}_{H_2O}}$), and H_2 consumption ($^{\Delta S^{\ddagger}_{H_2}}$) are calculated from the intercept of temperature dependencies of the respective formation rates (Figures S16-S19) normalized by surface Pd estimated by CO chemisorption values listed in Tables 1 and S1.

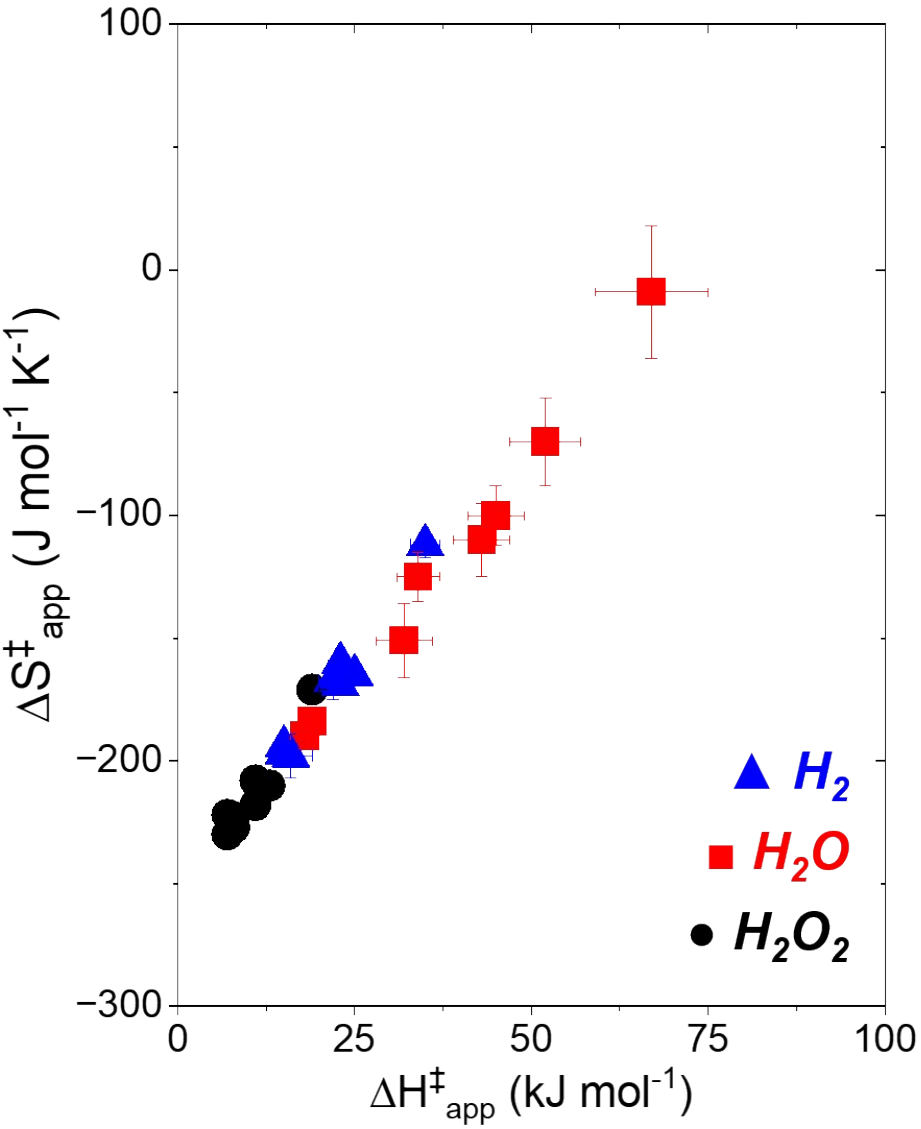

Figure S25. Entropy-enthalpy compensation effects between H_2O_2 (black ●) and H_2O (red ■) formation, and H_2 consumption (blue ▲).

Figure S25 shows a scatter plot relating $\Delta S^{\ddagger}$ to $\Delta H^{\ddagger}$ indicate that the kinetic parameters for H_2O_2 formation, H_2O formation, and H_2 consumption reactions show enthalpy-entropy compensation or a high degree of collinearity (i.e., the best fit lines to $\Delta S^{\ddagger}$ to $\Delta H^{\ddagger}$ for each reaction show nearly identical slopes and intercepts).

Section S8. Supplementary Catalyst Information, Characterization, and Kinetics

Table S2. Metal loadings, PZC values, H_2O_2 turnover rates and selectivities of catalysts not reported in the main text.

Catalyst	Pd Loading (wt%)	PZC	H_2O_2 TOR[a] (mol) (mol Pd s)$^{-1}$	H_2O_2 Selectivity[a] (%)
Pd- Fumed SiO_2	0.05	3.5 ± 0.5	0.058 ± 0.001	34 ± 1
Pd-TiO_2	0.05	3.5 ± 0.2	0.022 ± 0.001	32 ± 2

[a]measured at 200 kPa H_2, 60 kPa O_2, 286 K in deionized H_2O solvent.

Table S3. Activation barrier measurements of catalysts not reported in the main text.

Catalyst	$\Delta H^{\ddagger}_{H2}$ (kJ mol^{-1})	$\Delta H^{\ddagger}_{H2O2}$ (kJ mol^{-1})	$\Delta H^{\ddagger}_{H2O}$ (kJ mol^{-1})	$\Delta\Delta H^{\ddagger}$ (kJ mol^{-1})
Pd-SiO_2[a]	10 ± 1	9 ± 1	8 ± 2	0 ± 3
Pd-FAU[a]	18 ± 3	11 ± 3	22 ± 3	11 ± 5
Pd-Fumed SiO_2[b]	17 ± 1	8 ± 1	22 ± 1	14 ± 2
Pd-TiO_2 [b]	14 ± 1	0 ± 1	21 ± 1	21 ± 2

[a]measured at 55 kPa H_2, 80 kPa O_2, 276-296 K.

[b]measured at 200 kPa H_2, 60 kPa O_2, 276-296 K.

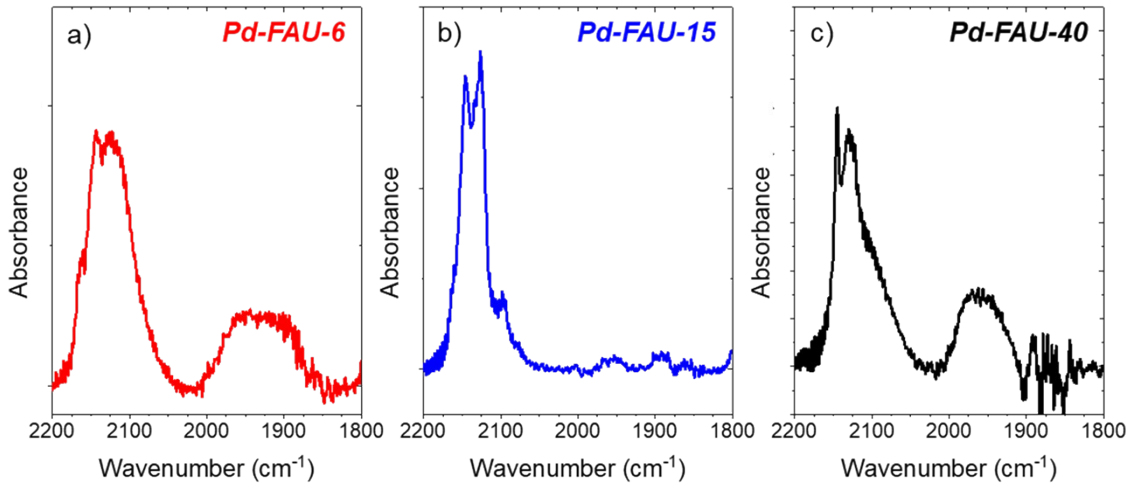

Figure S26. Infrared spectra of chemically adsorbed CO (0.1 kPa CO) on (a) Pd-FAU-6 (red), (b) Pd-FAU-15 (blue), and (c) Pd-FAU-40 (black) after reduction at 473 K.

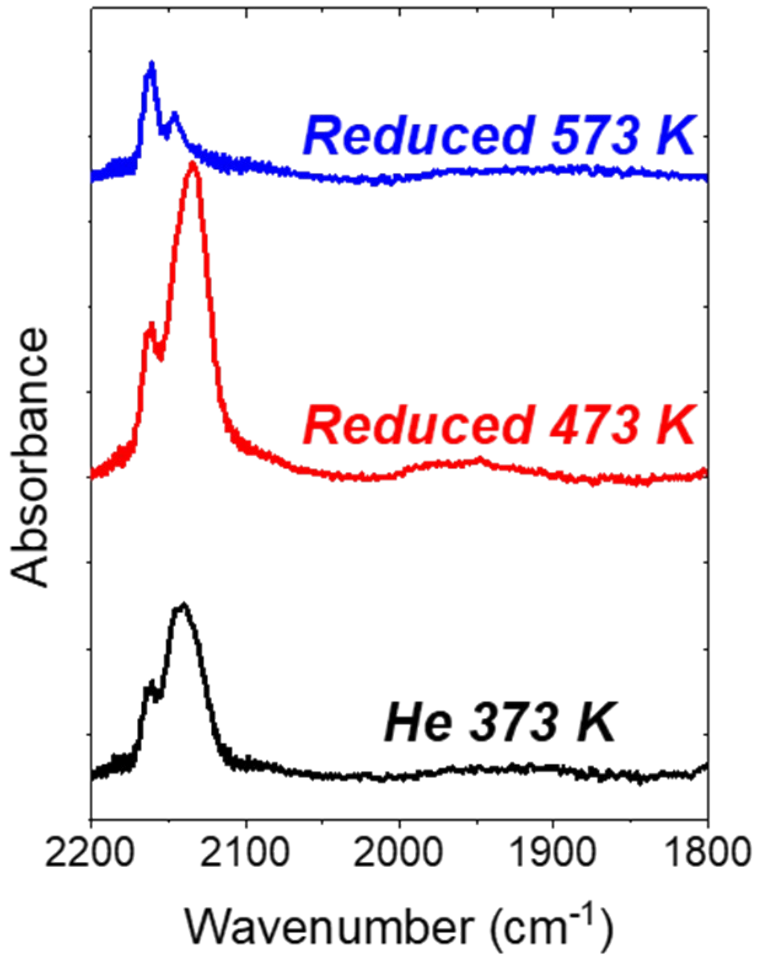

Figure S27. Infrared spectra of CO adsorbed (303 K, 0.1 kPa CO) to used oxidized Pd-FAU-15 after thermal treatments in He at 373 K (black), in 20 kPa H_2 at 473 K (red), 20 kPa H_2 at 573 K (blue) and 20 kPa O_2 at 373 K (green). Spectra are shown in ascending order. The sample was oxidized at 823 K, stabilized under reaction conditions for 12 h, and loaded into the infrared cell.

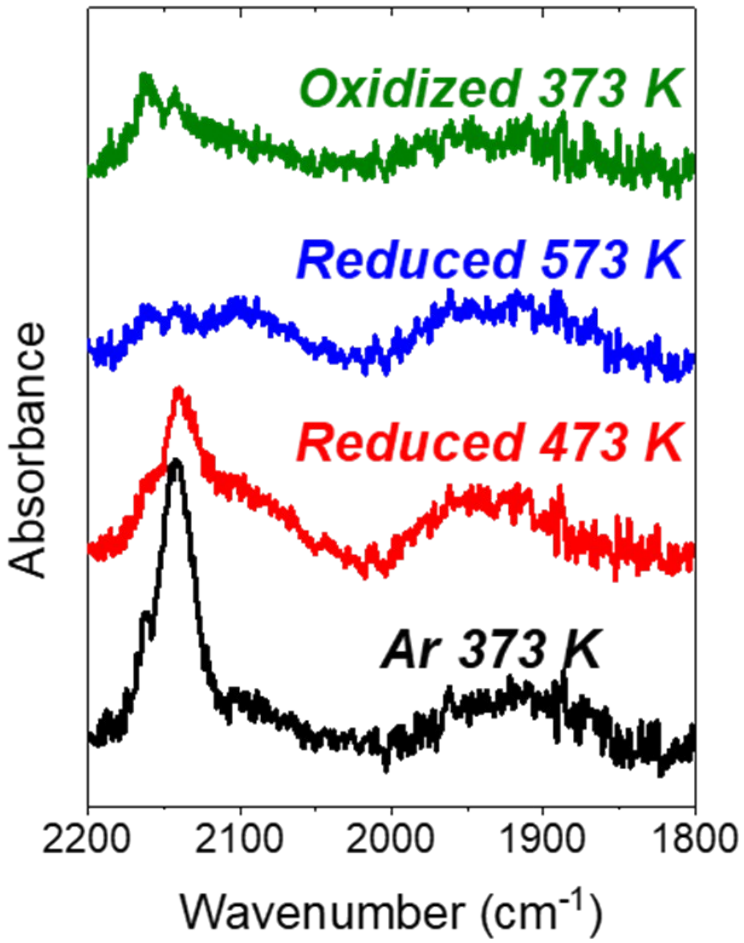

Figure S28. Infrared spectra of CO adsorbed (303 K, 0.1 kPa CO) to used reduced Pd-FAU-15 after thermal treatments in Ar at 373 K (black), in 20 kPa H_2 at 473 K (red), 20 kPa H_2 at 573 K (blue) and 20 kPa O_2 at 373 K (green). Spectra are shown in ascending order. The sample was reduced at 773 K, stabilized under reaction conditions for 12 h, and loaded into the infrared cell.

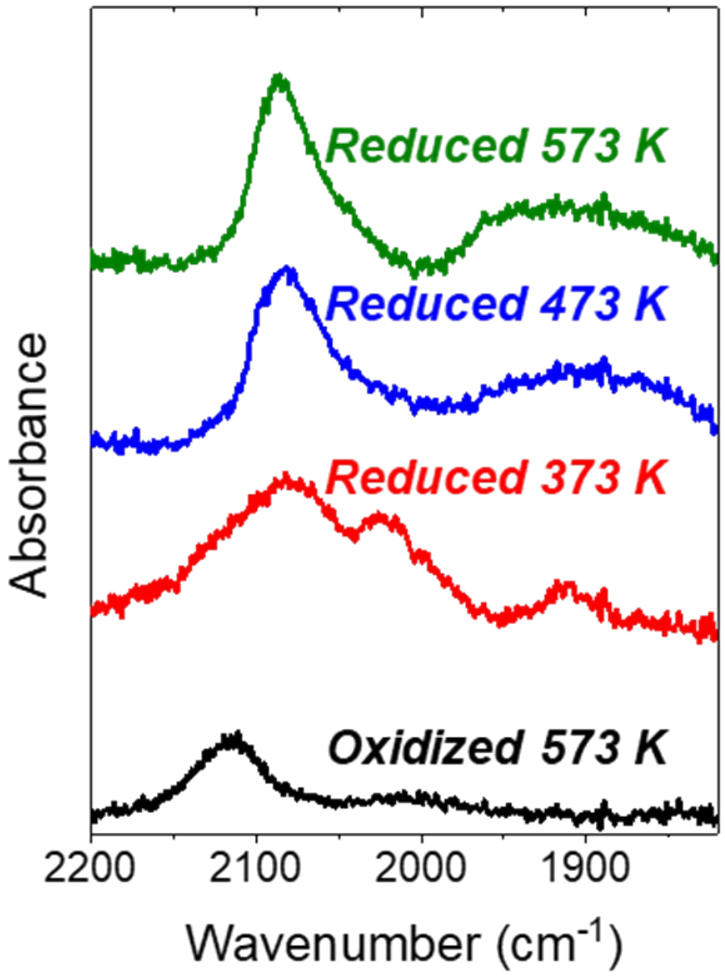

Figure S29. Infrared spectra of CO adsorbed (303 K, 0.02 kPa CO) to Pd-Al_2O_3 after thermal treatments in O_2 at 573 K (black), in 20 kPa H_2 at 373 K (red), 20 kPa H_2 at 473 K (blue) and 20 kPa H_2 at 573 K (green). Spectra are shown in ascending order.

REFERENCES

(1) Fagherazzi, G.; Benedetti, A.; Polizzi, S.; Di Mario, A.; Pinna, F.; Signoretto, M.; Pernicone, N. Structural investigation on the stoichiometry of β-PdHx in Pd/SiO_2 catalysts as a function of metal dispersion. *Catalysis letters* **1995**, *32* (3), 293-303.

(2) Krishnankutty, N.; Vannice, M. A. The effect of pretreatment on Pd/C catalysts: I. adsorption and absorption properties. *Journal of catalysis* **1995**, *155* (2), 312-326.

(3) Kugler, E.; Boudart, M. Ligand and ensemble effects in the adsorption of carbon monoxide on supported palladium-gold alloys. *Journal of Catalysis* **1979**, *59* (2), 201-210.

(4) Kunz, S.; Iglesia, E. Mechanistic evidence for sequential displacement–reduction routes in the synthesis of Pd–Au clusters with uniform size and clean surfaces. *The Journal of Physical Chemistry C* **2014**, *118* (14), 7468-7479.

(5) Noh, J. S.; Schwarz, J. A. Estimation of the point of zero charge of simple oxides by mass titration. *J. Colloid. Interf. Sci.* **1989**, *130* (1), 157-164.

(6) Park, J.; Regalbuto, J. R. A Simple, Accurate Determination of Oxide PZC and the Strong Buffering Effect of Oxide Surfaces at Incipient Wetness. *J. Colloid Interf. Sci.* **1995**, *175* (1), 239-252.

(7) Madon, R. J.; Boudart, M. Experimental criterion for the absence of artifacts in the measurement of rates of heterogeneous catalytic reactions. *Industrial & Engineering Chemistry Fundamentals* **1982**, *21* (4), 438-447.

(8) Wilson, N. M.; Flaherty, D. W. Mechanism for the Direct Synthesis of H_2O_2 on Pd Clusters: Heterolytic Reaction Pathways at the Liquid–Solid Interface. *Journal of the American Chemical Society* **2016**, *138* (2), 574-586. DOI: 10.1021/jacs.5b10669.

(9) Ricciardulli, T.; Gorthy, S.; Adams, J. S.; Thompson, C.; Karim, A. M.; Neurock, M.; Flaherty, D. W. Effect of Pd Coordination and Isolation on the Catalytic Reduction of O_2 to H_2O_2 over PdAu Bimetallic Nanoparticles. *Journal of the American Chemical Society* **2021**, *143* (14), 5445-5464. DOI: 10.1021/jacs.1c00539.

(10) Adams, J. S.; Chen, H.; Ricciardulli, T.; Vijayaraghavan, S.; Sampath, A.; Flaherty, D. W. Distinct Site Motifs Activate O_2 and H_2 on Supported Au Nanoparticles in Liquid Water. *ACS Catalysis* **2024**, *14*, 3248-3265.

(11) Adams, J. S.; Chemburkar, A.; Priyadarshini, P.; Ricciardulli, T.; Lu, Y.; Maliekkal, V.; Sampath, A.; Winikoff, S.; Karim, A. M.; Neurock, M. Solvent molecules form surface redox mediators in situ and cocatalyze O_2 reduction on Pd. *Science* **2021**, *371* (6529), 626-632.